Formation of a tropopause cirrus layer observed over Florida during CRYSTAL-FACE

Eric Jensen,[1] Leonhard Pfister,[1] Thaopaul Bui,[1] Andrew Weinheimer,[2] Elliot Weinstock,[3] Jessica Smith,[3] Jasna Pittman,[3] Darrel Baumgardner,[4] Paul Lawson,[5] and Mathew J. McGill[6]

Received 20 February 2004; revised 29 June 2004; accepted 11 November 2004; published 15 February 2005.

[1] On 13 July 2002 a widespread, subvisible tropopause cirrus layer occurred over the Florida region. This cloud was observed in great detail with the NASA Cirrus Regional Study of Tropical Anvils and Cirrus Layers–Florida Area Cirrus Experiment (CRYSTAL-FACE) instrumentation, including in situ measurements with the WB-57 aircraft. In this paper, we use the 13 July cloud as a case study to evaluate the physical processes controlling the formation and evolution of tropopause cirrus layers. Microphysics measurements indicate that ice crystal diameters in the cloud layer ranged from about 7 to 50 μm, and the peak number mode was about 10–25 μm. In situ water vapor and temperature measurements in the cloud indicated supersaturation with respect to ice throughout, with ice saturation ratios as large as 1.8. Even when the ice surface area density was as high as about 500 μm^2 cm^{-3}, ice supersaturations of 20–30% were observed. Trajectory analysis shows that the air sampled near the tropopause on this day generally came from the north and cooled considerably during the previous few days. Examination of infrared satellite imagery along air parcel back trajectories from the WB-57 flight track indicates that the tropopause cloud layer formation was, in general, not simply left over ice from recently generated anvil cirrus. Simulations of cloud formation using time-height curtains of temperature along the trajectory paths show that the cloud could have formed in situ near the tropopause as the air was advected into the south Florida region and cooled to unusually low temperatures. If we assume a high threshold for ice nucleation via homogeneous freezing of aqueous sulfate aerosols, the model reproduces the observed cloud structure, ice crystal size distributions, and ice supersaturation statistics. Inclusion of observed gravity wave temperature perturbations in the simulations is essential to reproduce the observed cloud properties. Without waves, crystal number densities are too low, crystal sizes are too large, and the crystals fall out too fast, leaving very little cloud persisting at the end of the simulations. In the cloud simulations, coincidence of high supersaturations and high surface areas can be produced by either recent nucleation or sedimentation of crystals into supersaturated layers. The agreement between model results and observed supersaturations is improved somewhat if we assume that the steady state relative humidity within cirrus at $T < 200$ K is enhanced by about 30%. The WB-57 measurements and the model results suggest that the cloud layer irreversibly dehydrated air near the tropopause.

Citation: Jensen, E., L. Pfister, T. Bui, A. Weinheimer, E. Weinstock, J. Smith, J. Pittman, D. Baumgardner, P. Lawson, and M. J. McGill (2005), Formation of a tropopause cirrus layer observed over Florida during CRYSTAL-FACE, *J. Geophys. Res.*, *110*, D03208, doi:10.1029/2004JD004671.

1. Introduction

[2] Thin, laminar cirrus layers are frequently observed near the tropical tropopause. Limb-viewing satellite measurements and nadir/zenith lidar measurements indicate that these clouds occur with frequencies as high as about 40% within the tropopause layer (TTL, about 15–19 km) in some parts of the tropics [*Comstock et al.*, 2002; *Wang et al.*, 1996]. There has been considerable interest in these clouds recently resulting from their potentially important role in dehydration of air entering the stratosphere in the

[1]NASA Ames Research Center, Moffett Field, California, USA.
[2]National Center for Atmospheric Research, Boulder, Colorado, USA.
[3]Department of Chemistry and Chemical Biology, Harvard University, Cambridge, Massachusetts, USA.
[4]Centro de Ciencias de la Atmosfera, Universidad Nacional Autonoma de Mexico, Mexico City, Mexico.
[5]Spec, Inc., Boulder, Colorado, USA.
[6]NASA Goddard Space Flight Center, Greenbelt, Maryland, USA.

0148-0227/05/2004JD004671

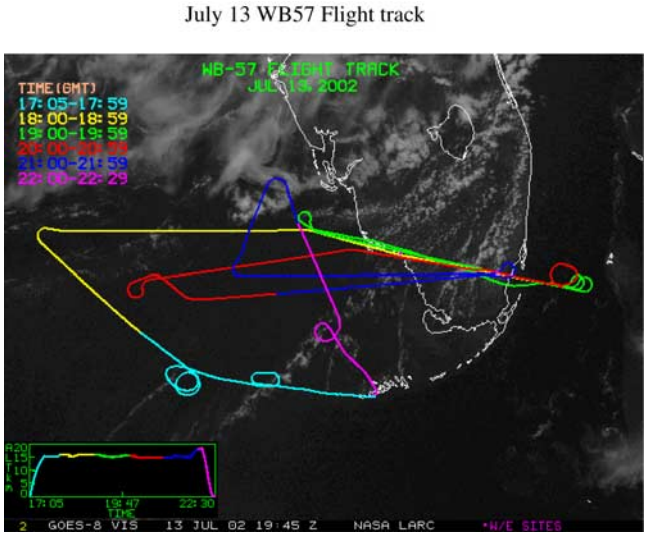

Figure 1. WB-57 flight track plotted over the 13 July, 1945 UTC, GOES visible satellite image. The inset shows the altitude of the aircraft versus time.

tropics [*Jensen et al.*, 1996; *Gettelman et al.*, 2002; *Jensen and Pfister*, 2004].

[3] *Pfister et al.* [2001] showed that thin cirrus near the tropical tropopause can either be remnants of anvil cirrus generated by deep convection or formed in situ because of cooling of air in the tropopause region. Modeling studies have evaluated the properties and effects of thin cirrus formation driven by slow ascent through the tropopause layer [*Jensen et al.*, 2001] and cooling along air parcel trajectories in the TTL [*Gettelman et al.*, 2002; *Jensen and Pfister*, 2004]. The cloud lifetimes and their effects on the TTL water vapor concentration depend on cloud processes and properties such as ice nucleation, ice crystal number densities, and crystal sizes.

[4] Very few direct measurements of the microphysical properties of these clouds have been made. *Heymsfield* [1986] reported in situ observations in a stratiform ice cloud at 16.2–16.7 km over the equator. Ice crystal replicator and Axially Scattering Spectrometer Probe measurements indicated ice number densities were at least 0.05 cm^{-3}, and the crystal lengths ranged from the minimum detectable size (4 μm) up to 50 μm. Recently, *Peter et al.* [2003] reported measurements of very thin cirrus layers just below the tropical tropopause. Forward Scattering Spectrometer Probe (FSSP-300) measurements indicated very low ice number densities ($5–10 \times 10^{-3}$ cm^{-3}) with diameters typically about 10–12 μm.

[5] In this paper, we report detailed measurements of a cirrus layer observed at the subtropical tropopause during the NASA Cirrus Regional Study of Tropical Anvils and Cirrus Layers–Florida Area Cirrus Experiment (CRYSTAL-FACE). On 13 July 2002 an extensive, optically thin cirrus layer was observed at the tropopause (14–15) km over the south Florida region. This cloud layer was sampled in detail with airborne in situ and remote-sensing instrumentation. In situ measurements were made with a large number of instruments on the WB-57 aircraft. Although the temperatures and water vapor concentrations in the subtropics are higher than those encountered in the tropics where dehydration of air entering the stratosphere is thought to occur, there are strong similarities between this cloud system and tropical thin cirrus. As we will show, formation of this cloud layer was driven by advection of air into a region of anomalously cold tropopause temperature in an anticyclonic motion. Similar dynamical processes drive thin cirrus formation in the tropical western Pacific [*Pfister et al.*, 2001].

[6] Our intent here is to use this case study to evaluate our understanding of the physical processes leading to the formation of these ice clouds. In the first section, we describe the CRYSTAL-FACE measurements of the tropopause cloud layer and the environmental conditions. Next, we evaluate the cloud formation mechanism, including the possibility that deep convection was involved. Last, we present results from detailed cloud model simulations driven by vertical profiles of temperature along back trajectories from the WB-57 flight track.

2. The 13 July Tropopause Cloud Layer Observations

[7] Most of the CRYSTAL-FACE flights were focused on convective systems and the cirrus anvils they produced [*Jensen et al.*, 2004]. On 13 July 2002 the forecast called for unusually suppressed convection over the Florida peninsula. In addition, very cold tropopause temperatures were predicted. Given the likelihood of tropopause cirrus formation under these conditions and the intermittent detection of thin cirrus at the tropopause by the micropulse lidar at the eastern ground site (Tamiami Airport), the ER-2 and WB-57 flights on this day were devoted to sampling the tropopause region over Florida.

[8] Figure 1 shows the flight track of the WB-57 overlaid on the 13 July, 1945 UTC, GOES visible satellite image. Over the southern Florida region, only small, shallow cumulus clouds were apparent. The ER-2 and WB-57 pilots attempted to fly in a stacked formation with the ER-2 as close to directly above the WB-57 as possible. This flight coordination allows direct comparison between the remote sensing and in situ measurements. Figure 2 shows time series of the ER-2 nadir Cloud Physics Lidar (CPL) [*McGill et al.*, 2004] backscatter as well as the WB-57 altitude and in situ measurements of particle surface area and nitric oxide. The tropopause cloud layer was present at 1–2 km below the cold-point tropopause throughout the flights. During much of the WB-57 flight, it was dipping into the top part of this cloud layer. The enhancements in particle surface area density (SAD) associated with ice crystals are apparent during the times when the WB-57 was in the cloud layer. When the aircraft flew well out into the Gulf, there appeared to be a deeper cloud layer with higher backscatter in the lower part of the cloud (see Figures 2 and 3).

[9] The horizontal extent of the optically thin cirrus layer is indicated by the Moderate Resolution Imaging Spectroradiometer (MODIS) 1.38 μm channel retrieval of thin cirrus optical depth [*Dessler and Yang*, 2003] shown in Figure 3. This image corresponds to the 13 July, 1330 UTC, Terra overpass. The MODIS data show that the thin cirrus layer extended well into the Atlantic and the Gulf. Retrieval of thin cirrus optical depth over the northern Gulf was not possible because of low-level clouds.

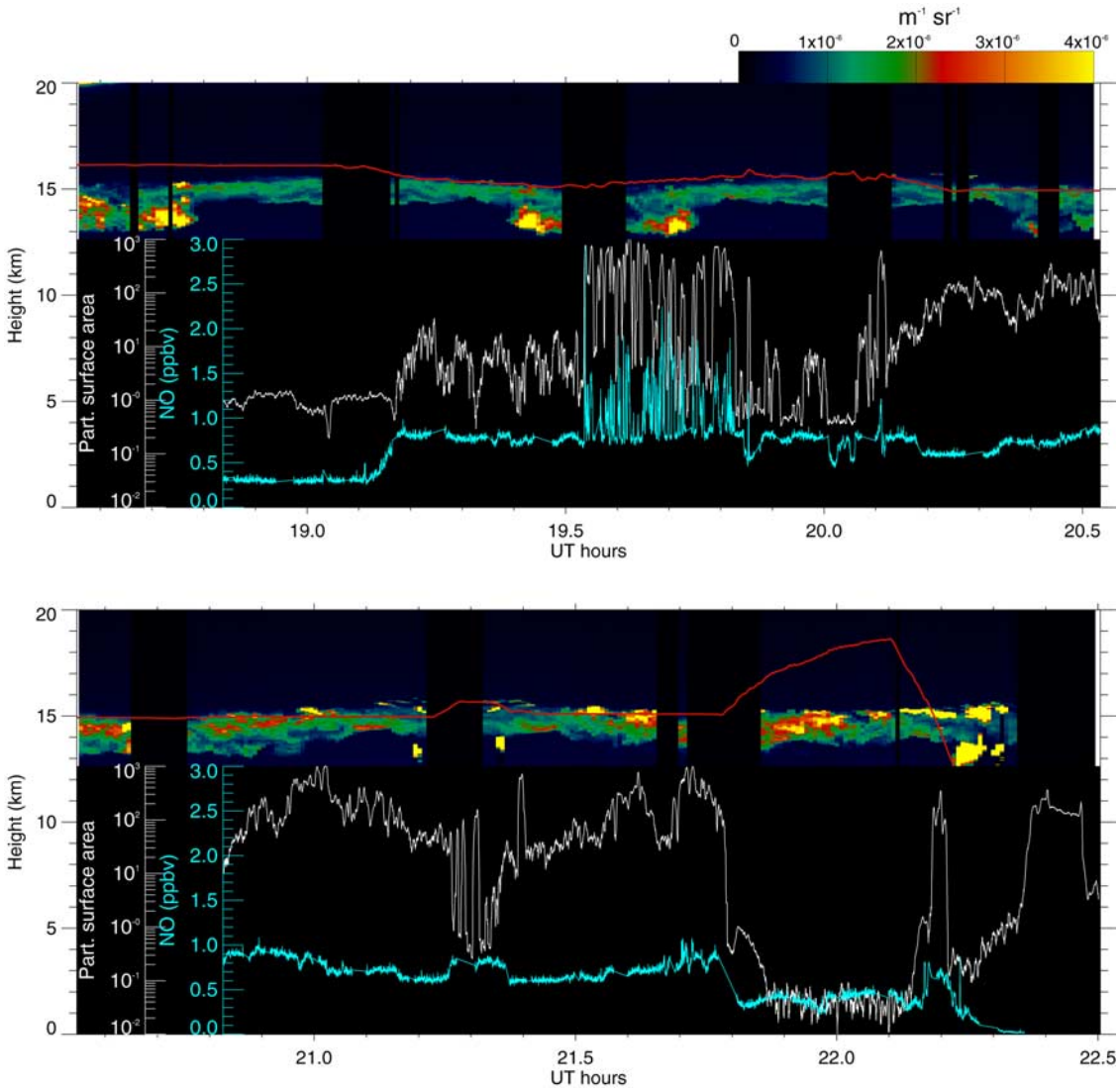

Figure 2. Tropopause cloud structure shown by the ER-2 nadir CPL lidar measurements of total attenuated backscatter at 532 nm. The red line indicates the WB-57 altitude, the in situ measurements of particle surface area density (μm^2 cm^3) are shown in white, and the NO concentration measured on the WB-57 is shown in cyan. The times when the aircraft dipped into the cloud correspond to enhancements in particle surface area associated with ice crystals.

[10] The WB-57 payload during the CRYSTAL-FACE mission included multiple instruments for sampling cloud properties, water vapor, temperature, and various tracers. The measurements used in this study include the Cloud, Aerosol, and Precipitation Spectrometer (CAPS) and the Scattering Spectrometer Probe (SPP-100) retrievals of aerosol and ice crystal size distributions [*Baumgardner et al.*, 2002]; the Harvard water vapor instrument (HWV) measurements of water vapor by photodissociating the H_2O molecules with 121.6 nm ($Lyman_\alpha$) radiation and detecting the resulting OH fluorescence at 315 nm [*Weinstock et al.*, 1994]; the Meteorological Measurement System (MMS) measurements of temperature and pressure; nitric oxide (NO) measurements [*Ridley et al.*, 2004]; and ozone measurements [*Richard et al.*, 2003].

[11] The WB-57 in situ measurements of temperature, water vapor mixing ratio, and particle surface area density are shown in Figure 4. Note that during one of the east-west legs across Florida, the WB-57 sampled its own persistent contrail. The contrail sampling is clearly indicated by the spikes in NO concentration from about 19.5 to 19.85 UT hours in Figure 2. Since we are focusing here on the natural cirrus layer, we have excluded this contrail sampling leg from our analysis. The following features are evident in Figure 4: (1) Minimum temperatures of 195–196 K occur at about $\theta = 360$ K (125 mbar). These tropopause temperatures are unusually cold for the Florida region during summertime. (2) Large supersaturations with respect to ice (saturation ratios of 1.2–1.8) are evident, particularly within the cloud layer at about $\theta = 354$–360 K indicated by the SAD enhancements. (3) There appears to be a layer of reduced water vapor mixing ratio at $\theta = 355$–365 K. The ozone profile from this flight (Figure 5) shows no evidence of interleaving air masses that might have caused the water vapor vertical structure. This apparently dehydrated layer is discussed further below.

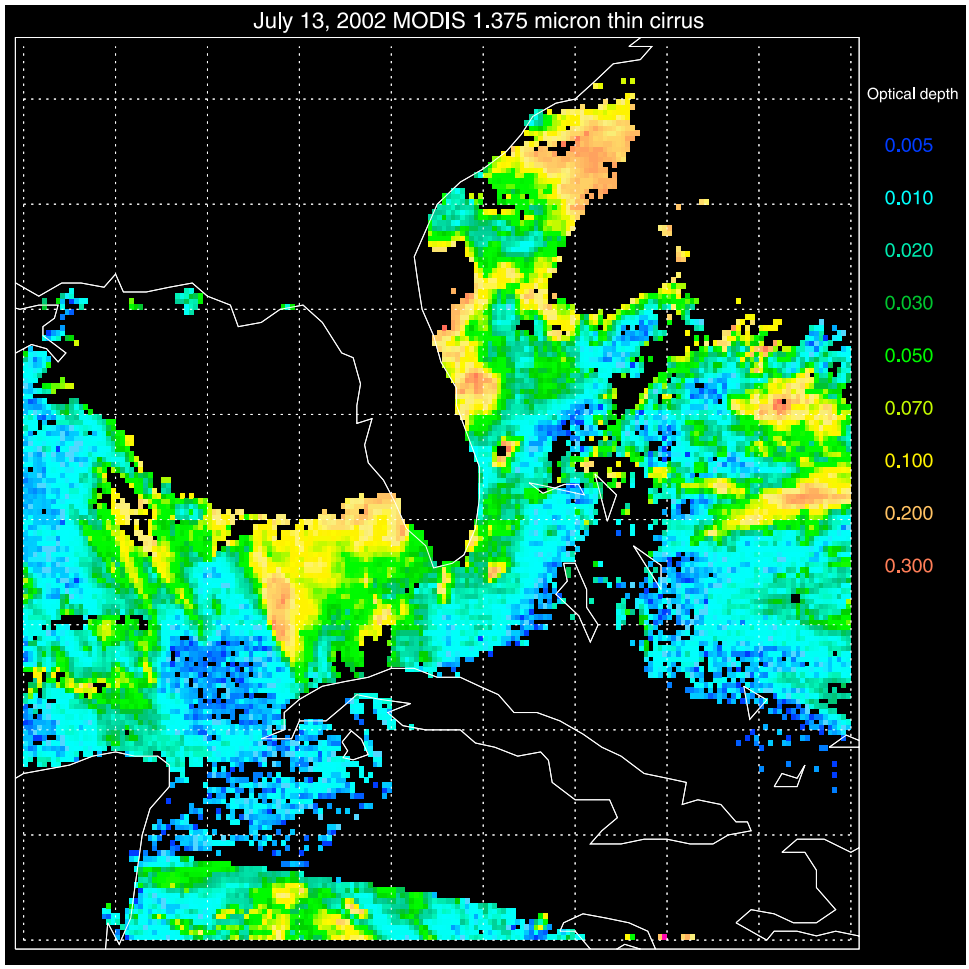

Figure 3. Terra MODIS 1.38 μm thin cirrus optical depth retrieval for the Florida region on the morning of 13 July. The MODIS data show that the thin cirrus layer was widespread over the southern Florida region.

[12] Figure 6 shows a composite size distribution constructed from CAPS and SPP-100 measurements. The particle measurements indicate highly variable crystal number density in the cloud, with peak number densities of about 0.32 cm^{-3} and typical number densities of about 0.05–0.1 cm^{-3} for particles larger than 4 μm diameter. The number distributions indicate a broad mode at diameters of about 10–25 μm, with smaller numbers of crystals as large as about 60 μm.

[13] The dependence of ice saturation ratio on particle surface area density is shown in Figure 7. When the aircraft was outside cloud, as indicated by SAD $\leq$ 2–3 μm^2 cm^{-3}, ice saturation ratios as high as about 1.6 were observed. These large clear-sky supersaturations are probably regions in which the temperature has not quite decreased enough to initiate freezing of supercooled sulfate aerosols. Even well within the cloud where surface area densities were as high as about 400 μm^2 cm^{-3}, the ice saturation ratios ranged from about 1.0–1.6, and at somewhat lower surface areas, saturation ratios as high as 1.8 were measured. These high supersaturations are qualitatively consistent with the high s_i threshold for freezing of sulfate aerosols (about 1.65) indicated by laboratory measurements [*Koop et al.*, 1998]. The highest values actually exceed those expected on the basis of the laboratory experiments; however, the uncertainty of the s_i measurement is about 10%. There is a great deal of scatter in the measured saturation ratios, and this scatter decreases only at SAD $\geq$ 400 μm^2 cm^{-3}. The s_i scatter even at high SAD is reasonable since the estimated precision of the saturation ratio measurement is about 5%, and measurements within a persistent contrail confirmed this precision [*Gao et al.*, 2004]. It is also noteworthy that the mean saturation ratio in regions well within the cloud (SAD $\geq$ 100 μm^2 cm^{-3}) is about 1.3.

[14] The in-cloud supersaturations as measured by the Harvard water vapor instrument can be systematically high because of evaporation of particles in the ram-heated instrument duct. Comparisons with the JPL hygrometer during CRYSTAL-FACE illustrated about 5% evaporation of the condensed mass on average. As shown by the gray points in Figure 7, the saturation ratios are only slightly affected by this evaporation. For the 13 July flight, the JPL/HWV comparisons suggest that the saturation ratios in the highest ice water content parts of the cloud may be overestimated by up to 10%. This error does not change the conclusions presented here. The existence of widely scattered saturation ratios and mean supersaturation within an ice cloud seems counterintuitive at first glance; the cloud

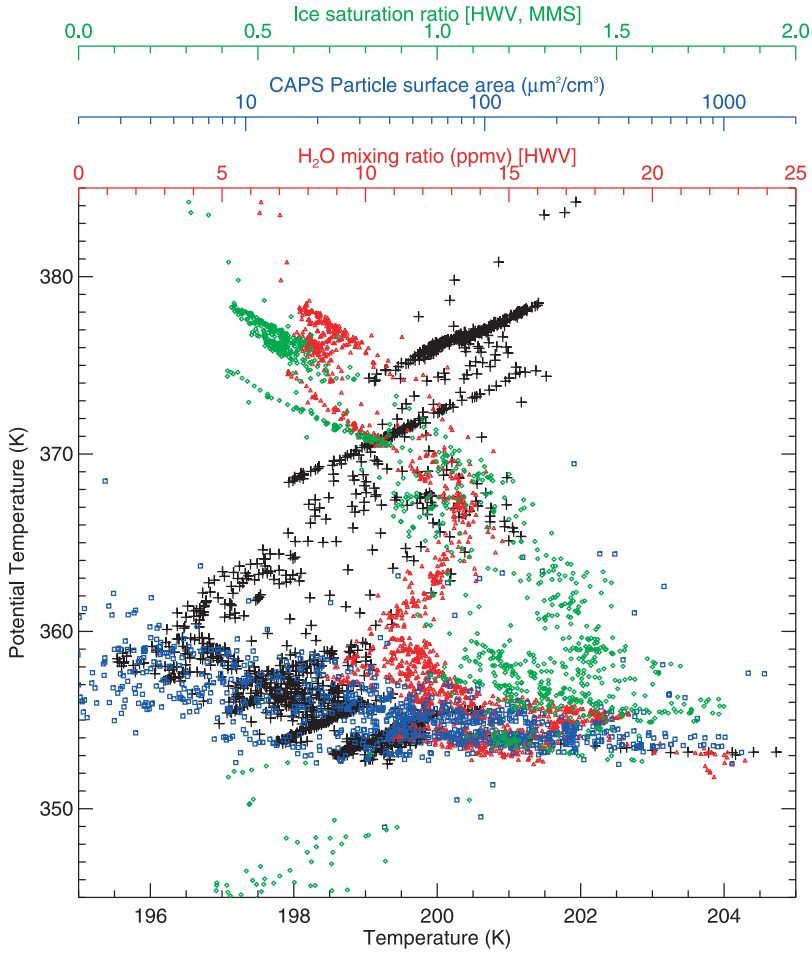

Figure 4. WB-57 in situ measurements of temperature (black), water vapor mixing ratio based on the Harvard water vapor measurement (red), ice saturation ratio (green), and particle surface area from the CAPS instrument (blue) plotted versus potential temperature. See text for details.

simulations below provide an explanation for these in-cloud supersaturations.

3. Convective Influence on Air Sampled by the WB-57

[15] The first-order issue regarding how the tropopause cloud layer formed is whether the cloud is left over from an anvil generated by deep convection or whether the cloud formed in situ within the upper troposphere. To evaluate the potential influence of convection, we have run 7-day isentropic back trajectories from times and locations along the WB-57 flight track during the cloud sampling. We used National Centers for Environmental Prediction (NCEP) wind and temperature fields for the trajectory calculations. Figure 8 shows that over the few days prior to 13 July, the air sampled generally came from the north and cooled substantially as it approached the southern Florida region. This cooling supports the plausibility that the cloud formed in situ in the uppermost troposphere.

[16] By combining the back trajectories and GOES infrared imagery, we have examined the possibility that the air sampled by the WB-57 was influenced by deep convection in the few day period before 13 July. This analysis indicates that most of the air sampled along the flight track did not encounter convection within the previous 1–2 days; however, much of the air sampled may have encountered convective injection within the past 2–5 days. The somewhat elevated NO concentrations (600–1000 pptv) also suggest that most of the region was influenced by convection within the past few days. Figure 9 shows examples of convective influence. The air sampled out over the Gulf may have been outflow from the previous day's convection over the Florida peninsula. This recent convective influence is consistent with the optically thick cloud somewhat below the tropopause cloud layer apparent in the CPL lidar image on the extreme western end of the flight track. The NO concentrations measured on the WB-57 also showed higher values (indicating more recent convective influence) on the western part of the east-west legs.

[17] Figure 9 also shows an example of a location over the peninsula that was influenced by convection along the coast of Georgia about 2 days earlier. The potential connection between ice injected near the tropopause by this convection and the observed tropopause cloud layer on 13 July is addressed by model simulations below.

4. Simulations of In Situ Cloud Formation

[18] For simulation of the tropopause cloud layer, we follow the approach used by *Jensen and Pfister* [2004]

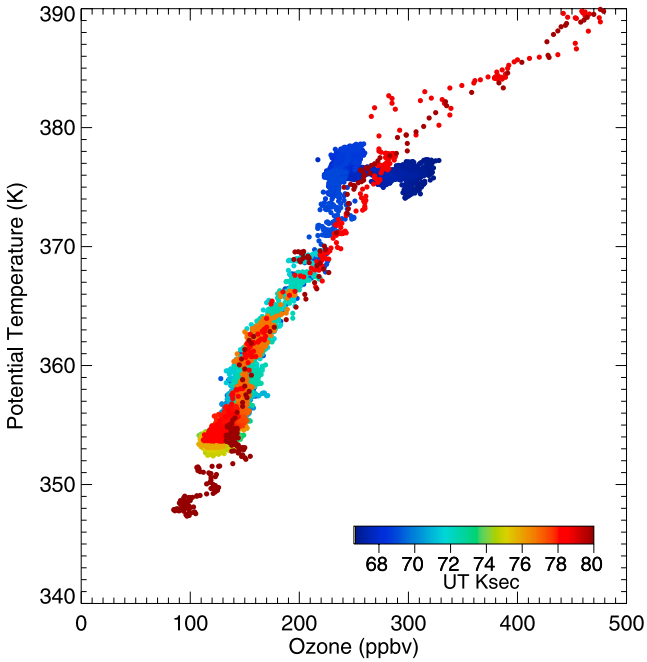

Figure 5. Ozone concentration measured on the WB-57 plotted versus potential temperature. If the dehydrated layer apparent in Figure 4 had been caused by interleaving of a dry layer with a different origin from the air above and below, then the ozone profile would not have shown such uniformity.

(hereinafter referred to as JP04) to simulate cirrus in the tropical tropopause layer with a one-dimensional model and temperature versus height and time taken from analysis fields along trajectories. The primary limitation of this approach is the neglect of wind shear. That is, we are implicitly assuming that the vertical column of air traveling along the trajectory at a particular potential temperature remains coherent over a period of hours-days. However, the model results presented below will show that the cloud layer was observed when it was probably only about 3–6 hours old. Hence it is unlikely that wind shear would have had a dramatic impact on the cloud structure.

4.1. Temperature Curtains Along Trajectories

[19] In order to simulate the tropopause cirrus formation, we need to determine the temperature histories of air parcels that ended up in the cloud layer. In addition, since ice crystal sedimentation may have significantly affected the cloud, we need temperature vertical profiles along the back trajectories. The approach used here is to extract temperature profiles from the NCEP analysis fields at each time point along the back trajectories (20 per day), resulting in a curtain of temperature versus time and height along the trajectory. We have generated such temperature/trajectory curtains from locations and times every 2.5 min along the WB-57 flight path during the 1716–2214 UT hours time period, resulting in 200 curtains.

[20] As described by JP04, the challenge to simulating tropopause cirrus using this trajectory-curtain approach is properly specifying the temperature profiles. This issue is particularly problematic for the subtropical region where the temperature minimum is located at about 125 mbar (see Figure 10) which is about halfway between the 100 and 150 mbar pressure levels in the NCEP analysis fields. Hence the analysis models do a very poor job of capturing the sharp temperature minimum, and large corrections are required to reproduce the tropopause temperature structure indicated by radiosondes. Fortunately, we had numerous temperature soundings in the south Florida region during CRYSTAL-FACE (see Figure 10), so we can at least accurately specify the temperature at the end of the simulations. The vertical grid used in our simulations (described below) has sufficient resolution to capture the sharp temperature minimum, but simply doing a spline interpolation of the analysis temperature profiles to our high-resolution grid does not produce the sharp temperature minimum. The soundings shown in Figure 10 also show the large amplitude temperature oscillations associated with gravity waves that are not represented in the analysis fields.

[21] We adjust the temperature curtains extracted from the analysis fields in a two-step process: First, we add in a pressure-, time-, latitude-, and longitude-dependent offset with peak amplitude at 125 mbar to represent the sharp tropopause structure and it's spatial/temporal variation. Second, we superimpose temperature oscillations associated with a spectrum of gravity waves. Figure 11 shows the spatial pattern of NCEP tropopause temperature at 1800 UT on 13 July. Comparison of the NCEP tropopause spatial and temporal patterns with radiosondes indicated a good correspondence of the locations and times with anomalously cold NCEP tropopause and a sharp cold temperature minimum in the soundings. (This correlation exists in spite of the fact that NCEP considerably overestimates the tropopause temperature.) Accordingly, we use the NCEP tropopause temperature field as a guide for estimating the spatial and temporal variability of the temperature perturbation. A two-dimensional Gaussian function, centered on 80.5°W longitude and 25° latitude, with longitude and latitude

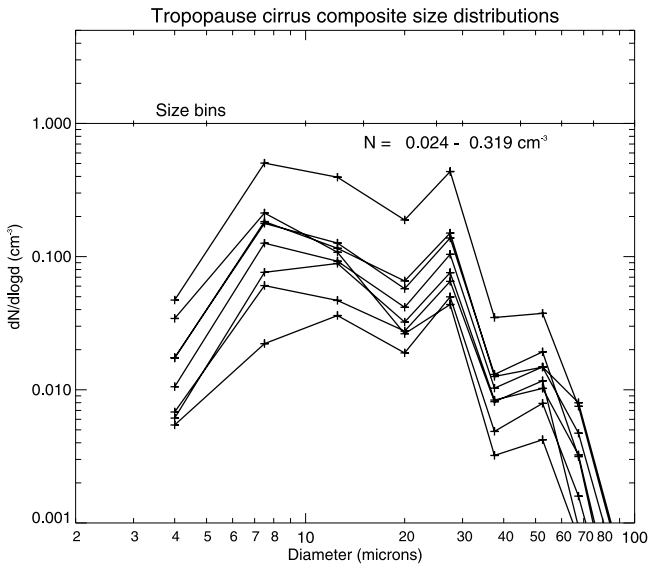

Figure 6. Composite particle size distributions during 600-s time periods when the WB-57 was sampling the tropopause cirrus layer.

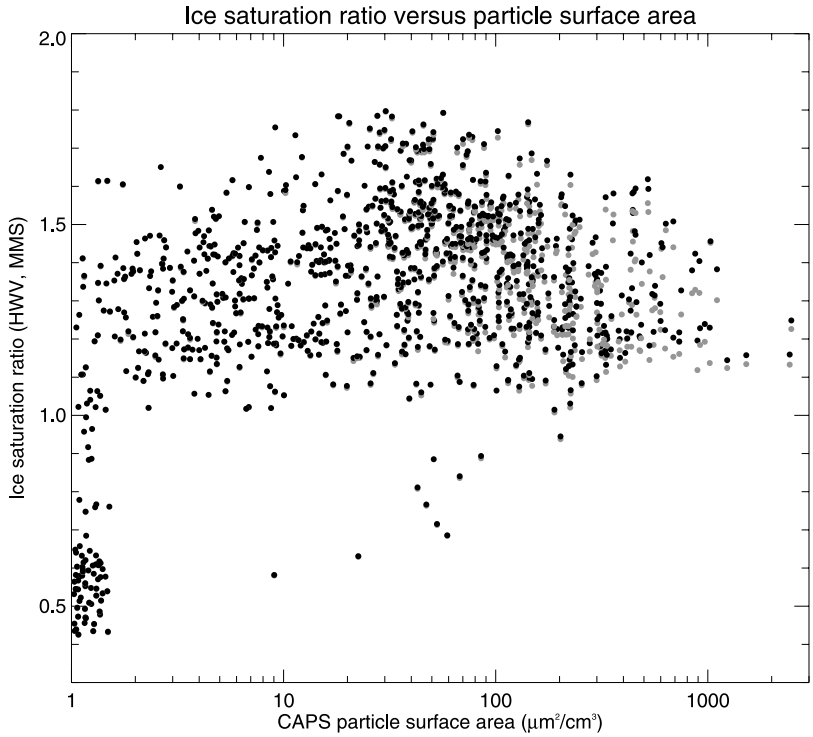

Figure 7. Ice saturation ratios (based on the Harvard water vapor and MMS temperature measurements) plotted versus total particle surface area density (taken from the CAPS measurements). Large ice supersaturations are evident at low-moderate surface area. The gray points show saturation ratios with 5% of the condensed mass (indicated by the Harvard total water instrument) subtracted to account for evaporation within the water vapor instrument inlet.

standard deviations of 15° and 7°, respectively, and rotated 30° counterclockwise, is used for the spatial variability. For the temporal variability, we linearly ramp up the perturbation amplitude for 12 hours starting at 1800 UT on 12 July, and keep the amplitude constant thereafter. The vertical profile of the perturbation is represented by a Gaussian centered on 122 mbar with a standard deviation of 10 mbar. An example of one of the resulting temperature curtains is provided in Figure 12. The offset produces the sharp temperature minimum at potential temperature (θ) of about 360 K (about 125 mbar) indicated by the southern Florida soundings (see Figure 10).

[22] The specification of wave-driven temperature oscillations follows the description given by JP04. This formulation includes a full spectrum Rossby-gravity waves, Kelvin waves, and higher-frequency gravity waves; however, at the latitudes under consideration here (≥20°), only the higher-frequency gravity waves are important. We have increased the amplitudes by a factor of 1.5 over what was used in JP04 to account for the ≃1–2 K amplitude in the uppermost troposphere indicated by the southern Florida soundings and the WB-57 temperature measurements. The result of superimposing the gravity wave temperature perturbations on the temperature curtain is shown in Figure 12. It is difficult to entirely represent the wave spectrum that affected the 13 July cloud layer. We only have limited information from the soundings and aircraft measurements, and the wave amplitudes and phases no doubt varied with location and time. The influence of the specified wave

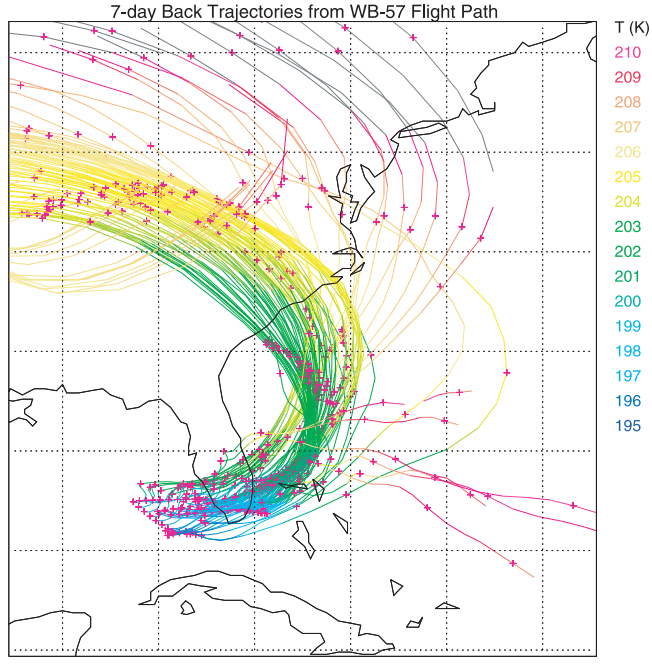

Figure 8. Back trajectories from locations along the WB-57 flight track shown on the basis of NCEP analyses. The colors indicate the minimum temperature in the vertical temperature profile at each location along the trajectories. The air sampled by the WB-57 generally came from the north and cooled rapidly as it approached the south Florida region.

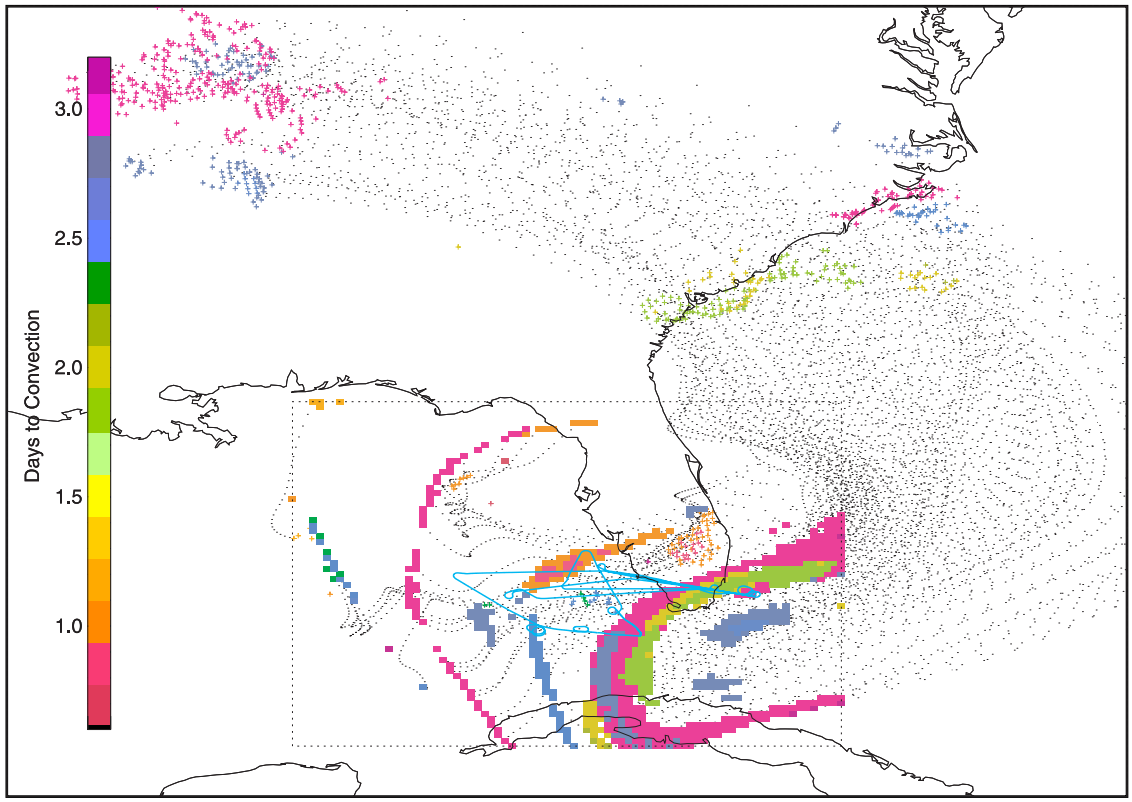

Figure 9. Convective influence analysis for 13 July, 2045 UTC. Convective sources are indicated by the colored "+" symbols, trajectories are shown with the black dotted lines, and the locations where the convectively injected air ends up at 2045 UTC are indicated by colored squares. The color coding indicates the age of convection. The WB-57 flight track is shown in cyan. In the Gulf, air along the flight track may have been influenced by the previous day's convection over the Florida peninsula (orange squares). At other locations along the flight, air appears to have come from the vicinity of convection 2–5 days previously.

temperature oscillations on the simulated cloud properties is described below.

4.2. Cloud Model Description

[23] For simulation of ice crystal nucleation, growth, and sedimentation of ice crystals, we use the cloud model described in detail by JP04. Essentially, this model tracks the growth and sedimentation of a large number of individual ice crystals in the vertical column. Water vapor concentration is calculated on a potential temperature grid ranging from 340 to 420 K (about 9–17 km) with a vertical resolution of 0.4 K (about 20 m at the tropopause). For each simulation, we must choose a horizontal cross-sectional area which the 1-D Lagrangian model represents. This area determines the number of ice crystals we will track to represent the cloud (see JP04 for details). For these simulations, we track several thousand ice crystals such that the cloud particle size distribution is statistically well represented.

[24] The physical processes treated in the cloud model are limited to ice nucleation, deposition growth, vertical advection of ice crystals and water vapor, and ice crystal sedimentation. Ice nucleation is assumed to occur via homogeneous freezing of aqueous sulfate aerosols as described below.

[25] For the initial aerosol size distribution, we use a lognormal with $N = 1000$ cm^{-3}, $r_o = 0.025$ μm, and $\sigma = 1.8$. Aerosols are depleted by ice nucleation, and the model time step is reduced sufficiently to capture the evolution of ice saturation ratio during the nucleation event, as described by JP04. As shown by previous modeling studies [e.g., *Jensen and Toon*, 1994], changes in the aerosol size distribution have very little impact on the number of ice crystals nucleated.

[26] The simplest assumption one can make about ice nucleation is that all of the aerosols are aqueous H_2SO_4. Laboratory studies have shown that ice nucleation in sulfate aerosols requires considerable supercooling below the ice frost point [e.g., *Bertram et al.*, 1996; *Koop et al.*, 1998]. Specifically, *Koop et al.* [1998] showed that at the temperatures of interest here ($T < 200$ K), saturation ratios with respect to ice exceeding about 1.65 are required for homogeneous freezing of sulfate aerosols. For this study, we use the parameterization for nucleation of ice in aqueous aerosols given by *Koop et al.* [2000].

[27] We must specify water vapor concentration profile at the initial times for each curtain. Using the NCEP analysis water vapor fields is problematic since no useful water vapor data are assimilated in the analysis model for the uppermost troposphere. Instead, we use the water vapor profile measured by the WB-57 in the south Florida region (see Figure 4) with the apparently dehydrated layer between $\theta = 355$ and 365 K filled in. The result is a water vapor

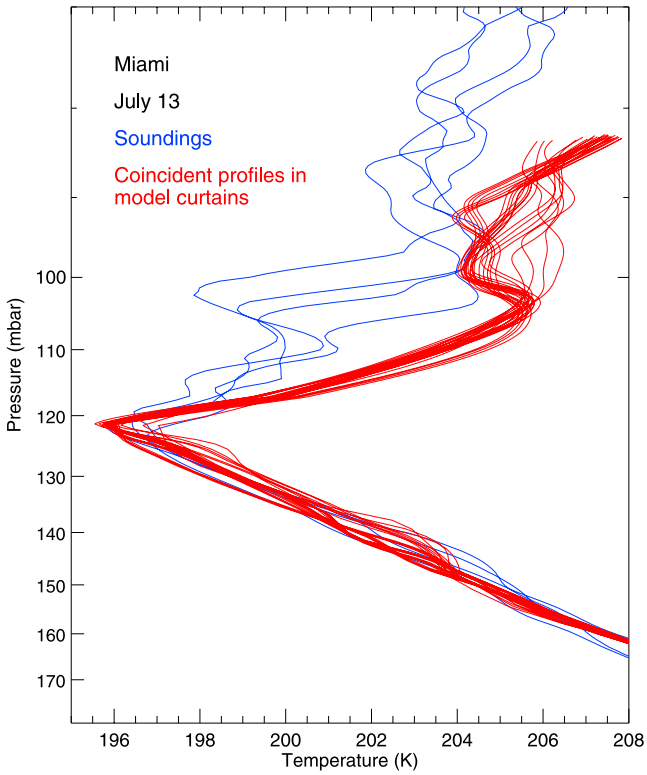

Figure 10. The 13 July 2002 Miami radiosonde temperature profiles (blue) and profiles from model temperature curtains including the corrections and gravity waves (red) that were coincident with the Miami sondes (within 8 hours and 50 km distance).

mixing ratio profile that decreases approximately linearly with height from about 20 ppmv at 355 K to 8 ppmv at 380 K. We are assuming here that this dehydrated layer was caused by the tropopause cloud layer we are trying to simulate, so upwind of the cloud, the dehydrated layer should have been filled in.

[28] The fraction of water molecules colliding with the ice crystal surface that actually get incorporated into the ice lattice, represented by the deposition coefficient, is generally assumed to be unity. *Gierens et al.* [2003] suggested the possibility that the deposition coefficient is much smaller than unity, and they showed that a small deposition coefficient would significantly increase ice number densities. We demonstrate the effects of a small deposition coefficient, α, on our model results below.

[29] *Gao et al.* [2004] used the CRYSTAL-FACE cirrus and contrail data to show that at temperatures below about 200 K, the in-cloud water vapor concentrations seem to converge toward a value about 30% higher than the saturation vapor pressure over ice. They suggest that nitric acid on the ice crystal surfaces may be inhibiting the deposition of H_2O from the vapor but not affecting sublimation, resulting in an adjusted steady state with supersaturated vapor. The crystal growth rate in cloud models (such as the one used here) is proportional to $p_{vap} - p_{sat}$, where p_{vap} is the ambient partial pressure of water vapor, and p_{sat} is the saturation vapor pressure over ice. To represent the effect suggested by *Gao et al.* [2004], we simply multiply p_{sat} by 1.3. The result is that at high ice surface areas the ice saturation ratio converges to a value of about 1.3 rather than 1.0.

[30] In the next section, we describe results from four sets of simulations. For the baseline case, we include gravity wave temperature oscillations and assume the deposition

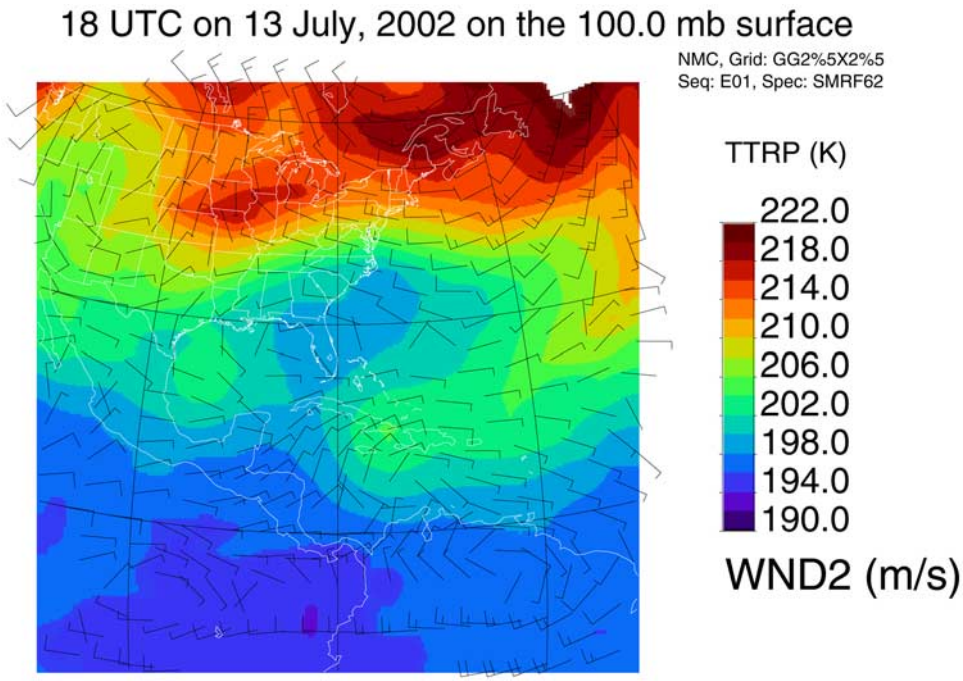

Figure 11. The 1800 UT, 13 July, NCEP temperature field. The spatial pattern of anomalously cold temperature over southern Florida corresponds to sharp temperature minima in radiosonde profiles.

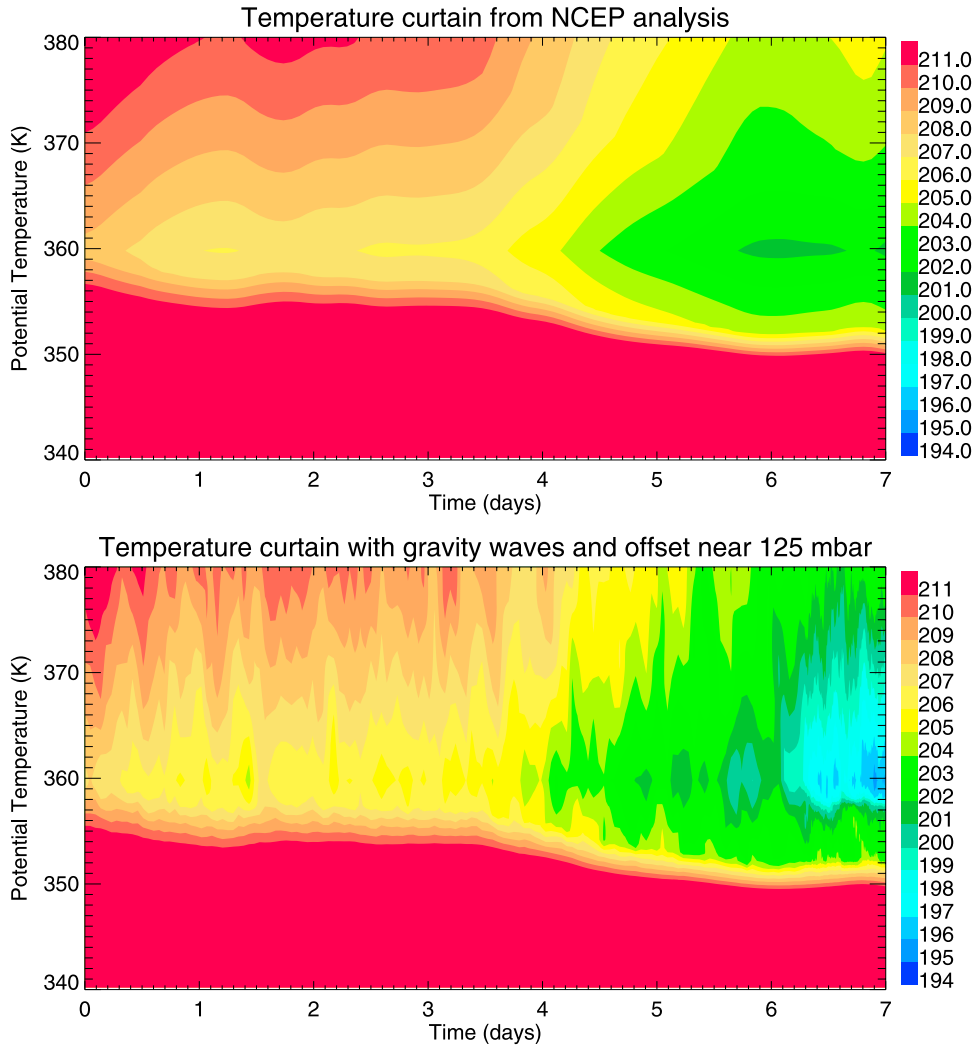

Figure 12. Examples of temperature curtains (top) without and (bottom) with the offset near the tropopause and gravity wave perturbations included.

coefficient is unity. As sensitivity tests, we have run sets of simulations (1) without wave-driven temperature oscillations, (2) with a deposition (and sublimation) coefficient of 0.05, and (3) with the *Gao et al.* [2004] effect included (see Table 1). Sets of 200 simulations (one for each curtain) were run for each case.

4.3. Model Results

[31] Figure 13 shows the evolution of ice saturation ratio, water vapor, ice crystal number density, and ice surface area density for the last 24 hours of a typical curtain from the baseline set of simulations. There are multiple nucleation events apparent: one at about 14 hours before the sampling time and a few others occurring in the last few hours of the simulation. The ice nucleated 14 hours earlier grows and falls out of the TTL within a few hours leaving behind dehydrated air below $\theta = 360$ K. Then, near the end of the simulation rapid cooling driven by gravity waves drives nucleation of ice number densities as high as about 0.5 cm^{-3} above 360 K, the crystals quickly grow to diameters of about 10–30 μm, and sediment down to about 358 K, resulting in about a 1-km-thick cloud layer. The dehydration of the layer above the cloud from about 358 to 362 K is apparent.

[32] For comparison with the observed cloud structure indicated by the lidar data (Figure 2), we have combined the final profiles from simulations ending at successive points along the aircraft flight path to generate cloud fields versus height and distance along the flight path. We have thus generated longitude-height plots for each of the

Table 1. Simulations and Results

Case	N_{ice},[a] cm^{-3}	SAD_{mean}, μm^2 cm^{-3}	SAD_{max}	Notes
Baseline	0.058	63.1	454	continuous tropopause cloud
No waves	0.00009	2.6	19	little or no cloud
$s_{i,eq} = 1.3$[b]	0.46	138	1016	continuous cloud
$\alpha = 0.05$[c]	5.5	545	3161	cloud more extensive than observed

[a]The ice number density is calculated as the mean for all times and grid cells from the last 3 hours of the 7-day simulations wherever $N_{ice} > 10^{-5}$ cm^{-3}.

[b]To approximate the effect indicated by *Gao et al.* [2004], we have artificially increased the saturation vapor pressure over ice by 30% such that the cloud comes to equilibrium with $s_i \simeq 1.3$.

[c]Deposition coefficient reduced to 0.05 as suggested by *Gierens et al.* [2003].

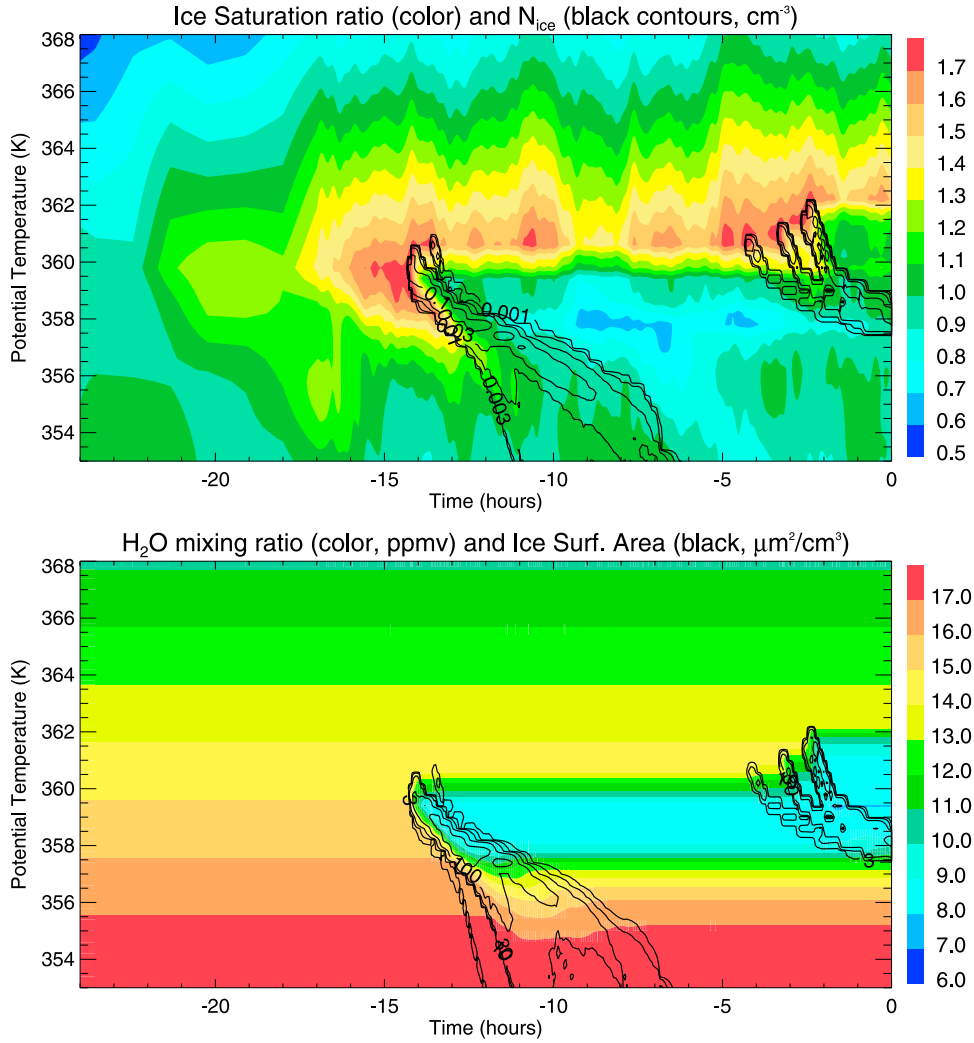

Figure 13. Fields plotted versus time and potential temperature for a typical cloud simulation. (top) Ice saturation ratio (color) and ice number density (black contours, cm^{-3}); (bottom) water vapor mixing ratio (color) and ice surface area densities (black contours, $\mu m^2\ cm^{-3}$).

roughly east-west legs that the aircraft made (see Figure 1). Figure 14 shows the result for one of these flight legs (the others look similar). The simulations reproduce the continuous cloud layer at around 357–360 K indicated by the lidar data. Surface areas in the simulated cloud are also comparable to the measured surface areas (≃10–300 $\mu m^3\ cm^{-3}$). The layer of dehydrated air centered at about 360 K is caused by ice crystal nucleation and growth at this level upstream. By the end of the trajectory simulations, most of the ice mass was below 360 K, with the layer near 360 K irreversibly dehydrated.

[33] The average ice crystal size distributions within cloud from the different sets of simulations are shown in Figure 15. As discussed above, there are large uncertainties in particle size distribution measurements for diameters smaller than about 6 μm; hence we focus our comparisons between model results and measurements on larger crystals. The model size distributions for the baseline case look very similar to the measured size distributions shown in Figure 6. The ice concentrations are comparable, and both distributions include number modes near 10–25 μm.

[34] In the simulations without waves, the slow, synoptic-scale cooling results in low ice concentrations (generally much less than 0.01 cm^{-3}). The crystals quickly grow to diameters of 40–50 μm and fall out of the supersaturated layer. The result is a patchy cloud with ice concentrations much lower than those observed. Reducing the deposition/sublimation coefficient from unity to 0.05 decreases the growth rates of small crystals. Hence the first ice crystals nucleated cannot drive down the supersaturation as quickly, and more crystals nucleate, resulting in much higher ice crystal concentrations: $N_{ice} \simeq 5\ cm^{-3}$ with $\alpha = 0.05$ rather than $N_{ice} \simeq 0.06\ cm^{-3}$ with $\alpha = 1$. Ice crystal growth is limited because of competition with the high ice concentrations. In contrast to the measured size distributions, the average crystal size distribution from the $\alpha = 0.05$ simulations shows a mode at diameters less than 10 μm and little or no ice at diameters greater than 20 μm. *Kärcher and Ström* [2003] also showed that cloud simulations gave poor agreement with measured ice number densities if a deposition coefficient significantly less than unity were assumed.

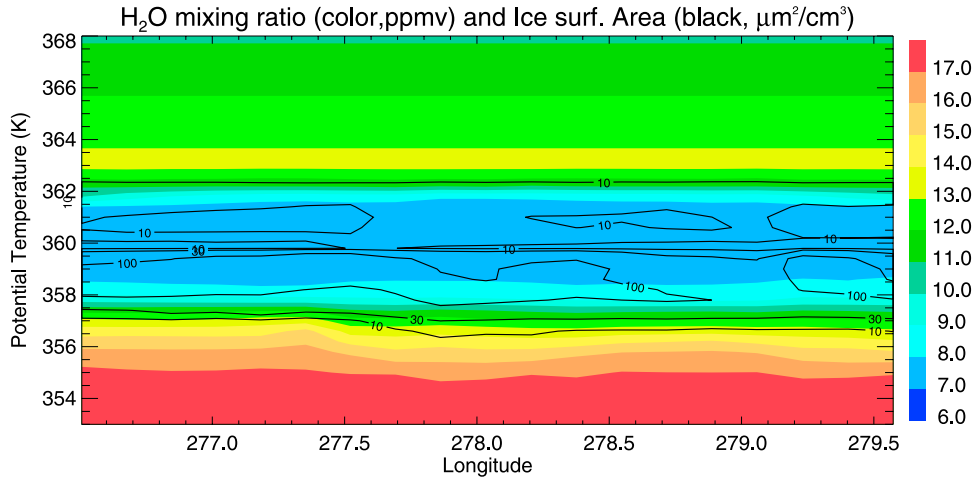

Figure 14. Simulated cloud fields plotted versus longitude and potential temperature for one of the east-west legs across southern Florida. These fields were constructed by combining the final profiles from several curtain simulations ending along the flight leg. The model reproduces the continuous cloud near the tropopause indicated by the lidar data.

[35] Increasing the steady state H_2O concentration in ice clouds (by artificially increasing the vapor pressure over ice) also results in about a factor of 2 higher ice concentrations and somewhat smaller crystals. However, the shift in the peak size mode is not dramatic, and given the uncertainties in size distribution measurements and the simulation temperature histories, the agreement with data in the enhanced s_i set of simulations is equivalent to that in the baseline case.

[36] As discussed in section 3, air sampled near the tropopause at several locations was likely affected by deep convection on previous days. This convective influence introduces the possibility that the tropopause cirrus layer is simply remaining ice that was injected by the cumulo-

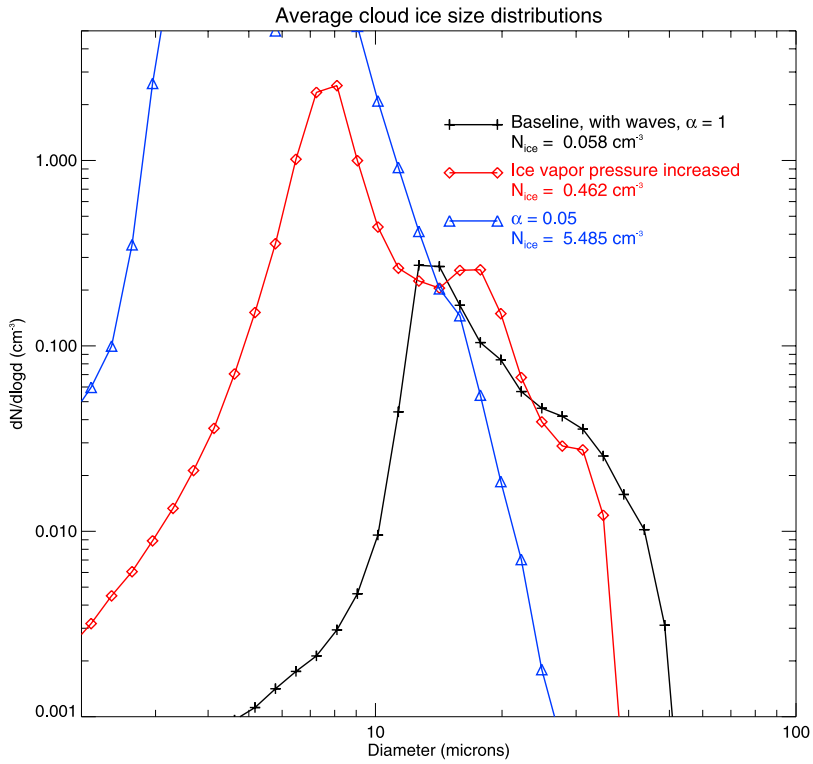

Figure 15. Model ice crystal size distributions averaged over all locations within the cloud at the final time. Size distributions are shown for baseline simulations with waves (black), simulations with increased vapor pressure over ice (red), and simulations with reduced deposition/sublimation coefficient (blue).

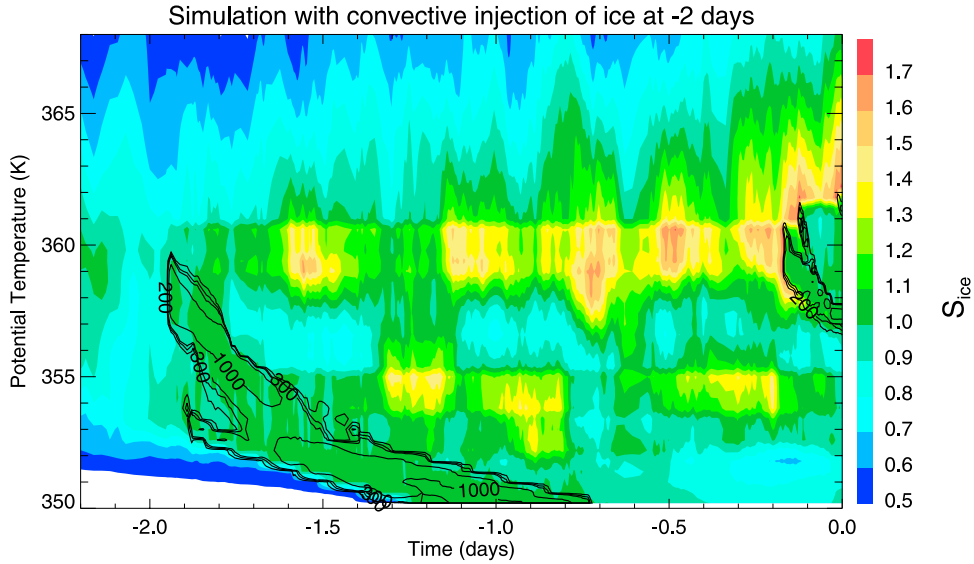

Figure 16. Ice saturation ratio (color) and ice water content (black contours) fields plotted versus time and potential temperature for a simulations with injection of ice crystals at the time when the back trajectory encountered deep convection (2 days before the end of the simulation). Any convectively generated ice crystals would have fallen out long before the air column reached southern Florida. See text for discussion.

nimbus clouds. To evaluate this issue with our model, we have run a few simulations in which the ice crystals are inserted in the model at the time of encounters with convective systems along the back trajectories.

[37] Figure 16 shows the cloud evolution in one of these simulations. At 5 days into the simulation (2 days before the trajectory reached the WB-57 flight track), ice crystals are injected between $\theta = 357$ and 361 K with a number density of 1 cm^{-3} and diameters randomly distributed between 10 and 30 μm. The ice crystals rapidly saturate the air by sublimating slightly. Then as the air continues to cool as the column approaches Florida, the ice crystals grow and fall, eventually sublimating at lower altitudes before the air column reaches the observation region. Even if we inject higher numbers of smaller crystals at the time of the convective influence, they grow to sizes >10 μm relatively quickly since the air continues cooling. A 20 μm diameter ice crystal will fall about 2.6 km in 2 days, so it is implausible that the thin cloud layer observed just at the tropopause was left over from convective injection days before. Toward the end of the simulation, an ice cloud forms in situ near the tropopause just as it did in the simulations without convective injection.

4.4. Cloud Supersaturation

[38] An observation that has received considerable attention is the high supersaturations with respect to ice measured by the WB-57 instrumentation within cold cirrus [*Gao et al.*, 2004]. The saturation ratios were particularly high in the very cold 13 July tropopause cirrus layer (see Figures 4 and 7). *Gao et al.* [2004] have used the CRYSTAL-FACE cirrus and contrail data to argue that nitric acid deposited on ice crystal surfaces at low temperatures may inhibit deposition of water vapor on ice, allowing the persistence of large ice supersaturations. We will first discuss issues concerning ice saturation measurements and processes that can lead to in-cloud supersaturation; next, we specifically compare supersaturations in the 13 July case study simulations with measurements.

4.4.1. Supersaturation Driven by Temperature Variability

[39] An initial concern with the relative humidity measurements is that the 1 Hz WB-57 in situ water vapor and temperature measurements represent averages over about 200 m along the flight path. There will always be some degree of fluctuation in temperature and water vapor concentration on smaller scales. Since the vapor pressure over ice has a nonlinear dependence on temperature, using the average temperature and average water vapor concentration to calculate relative humidity does not give the same answer as averaging the instantaneous relative humidities. In fact, using the average temperature and water vapor concentration gives an apparent supersaturation. However, for reasonable assumptions about the variability of temperature on scales smaller than 200 m, this apparent supersaturation is very small. For example, even if the amplitude of small-scale temperature variability was as high as 5 K, the apparent supersaturation would only be about 2%. Using the 20 Hz Meteorological Measurement System temperature measurements on the WB-57, we find that the standard deviation of temperature variability with frequencies higher than 1 Hz is less than 0.05 K, so the 1 Hz data should be entirely adequate for calculating relative humidity.

[40] One possible mechanism for generating large supersaturations within cloud is rapid temperature fluctuations that drive up the supersaturation faster than it can be depleted by crystal growth. The rate at which existing ice crystals can quench buildup of supersaturation in cooling air depends upon the total ice surface area density and the particle size distribution. Using the model size distributions from the baseline simulations, we have calculated the timescale for reduction of vapor in excess of ice saturation

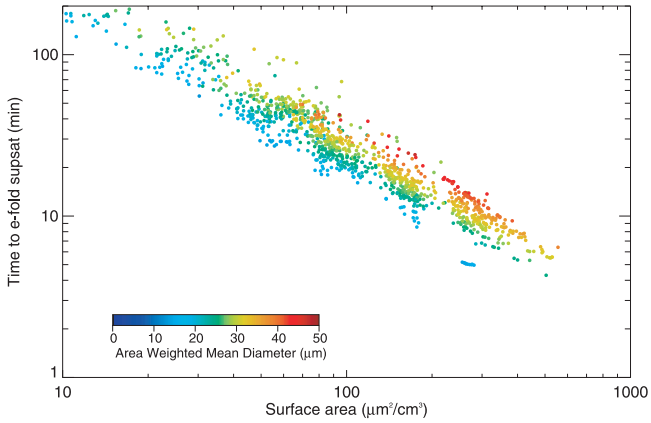

Figure 17. The *e*-folding time for supersaturation reduction due to ice crystal growth plotted versus ice crystal surface area. Ice crystal size distributions from the simulations were used for these calculations (see text).

defined as $\tau_g = S_i/(dS_i/dt)$ due to growth of ice crystals, where $S_i = s_{ice} - 1$ is the supersaturation with respect to ice. This timescale is simply the *e*-folding time for reduction of the ice supersaturation. Figure 17 shows the supersaturation relaxation time versus surface area. For surface areas greater than about 50 μm^2 cm^{-3}, the relaxation time is less than about 40 min. Since the clouds generally began forming a few hours before the final times in the simulations, one might expect that the ice supersaturation should be mostly depleted in the regions with relatively high surface area. However, as shown below, the cloud simulations do include locations with moderately high surface areas and high supersaturations (in agreement with the measurements).

[41] To quantitatively evaluate how effectively gravity waves can drive supersaturation, we set up an idealized simulation with a preexisting cloud layer and imposed high-frequency wave fluctuations. The cloud layer consisted of 0.09 cm^{-3} 10 μm ice crystals with a corresponding surface area of about 100 μm^2 cm^{-3}. Within the cloud layer near the temperature minimum, we set the initial ice saturation ratio to 1.0. To simplify the idealized simulation, we did not allow ice crystal sedimentation or vertical transport of water vapor. A spectrum of gravity wave temperature perturbations was imposed resulting in a peak-to-peak temperature oscillation of about 3 K. This amplitude is somewhat larger than the wave amplitude indicated by Miami soundings (Figure 10).

[42] Figure 18 shows the temperature and ice saturation ratio evolution at a particular vertical level in the idealized cloud simulation. Rapid temperature increases (decreases) drive decreases (increases) in ice saturation ratio since the ice crystals cannot sublimate (grow) rapidly enough to compete with the decrease (increase) in saturation driven by the temperature changes. During periods with little or no temperature change, the saturation ratio relaxes toward 1.0. The temperature fluctuations do not drive the supersaturation above about 10%, nor do they result in a time-averaged saturation ratio significantly above 1.0. Outside the cloud, the temperature oscillations drive supersaturations as high as 30%, so the cloud layer with 100 μm^2 cm^{-3} is sufficient to prevent buildup of large supersaturations with this level of temperature variability. We conclude from this experiment that the high in-cloud maximum supersaturations and average supersaturations of 20–30% in the observed and simulated 13 July cloud case are not caused solely by gravity wave temperature oscillations.

4.4.2. Supersaturation in the 13 July Case Study

[43] Next, we examine the supersaturations in the 13 July case study simulations. Figure 19 shows the model ice saturation ratio versus ice surface area (analogous to Figure 6) taken from the last 3 hours of the baseline simulations. To allow a more direct comparison with the measured ice saturation ratios, we have added normally distributed random values with a 5% standard deviation to the model saturation ratios. The model s_{ice} values are scattered between 1.0 and 1.7 for surface area densities up to about 50 μm^2 cm^{-3}; then at higher SAD the s_{ice} decreases

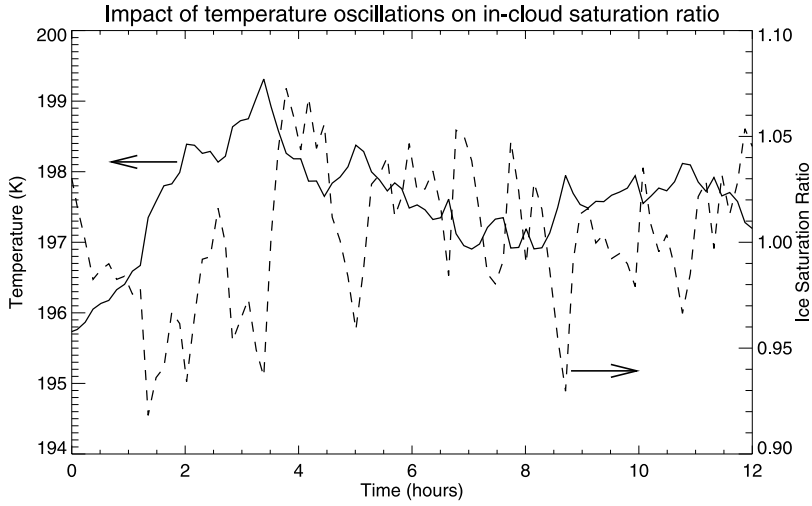

Figure 18. Temperature (solid line) and ice saturation ratio (dashed line) plotted versus time in an idealized simulation to test the effect of temperature oscillations on ice saturation ratio in a preexisting cloud initially at equilibrium (s_{ice} = 1.0). Using temperature variability similar to the observed 13 July variability, supersaturations no larger than about 5–10% occur within the cloud.

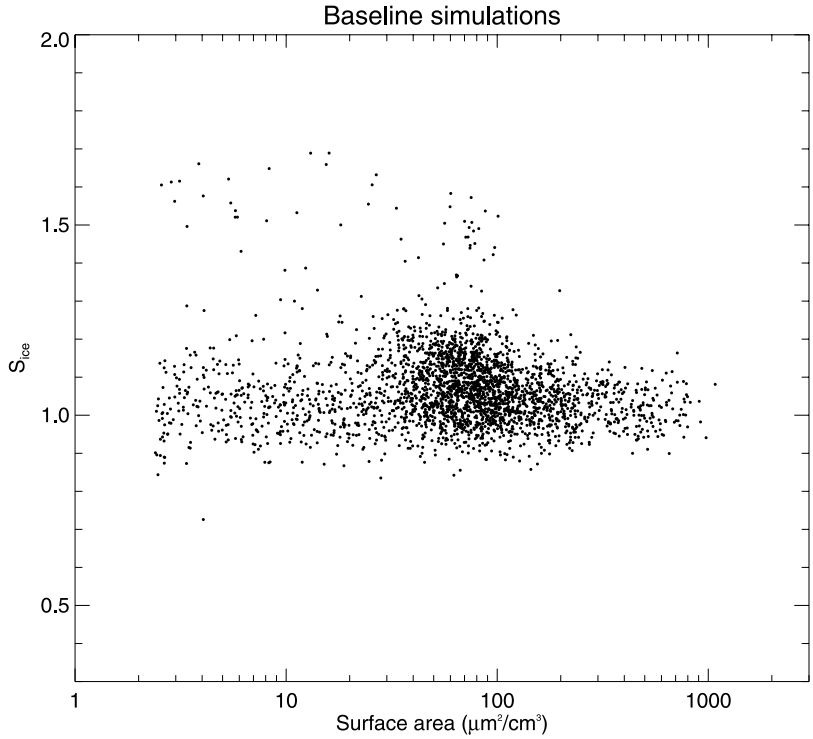

Figure 19. Ice saturation ratio plotted versus ice surface area for the baseline set of simulations. The s_{ice} is confined near 1.0 only when the surface areas exceed about 400 μm^2 cm^{-3}.

until at SAD $\geq$ 200 μm^2 cm^{-3} s_{ice} is confined to values near 1.0. The model results differ from the measurements in a few respects: First, the peak measured supersaturations ($s_{ice} \simeq 1.8$) are a bit larger than those in the simulations. Second, the measured s_{ice} converges toward about 1.2–1.3 at high SAD, whereas s_{ice} converges to near 1.0 in the baseline simulations. The model saturation ratios also seem to converge toward the equilibrium value at lower SAD than in the observations. However, if we include the last 4 hours of the simulated results instead of only the last 3 hours, elevated supersaturations extend out to SAD values of about 400 μm^2 cm^{-3} in agreement with the measurements. Given the uncertainty in the timing of the final cooling resulting in the cloud formation, the simulated s_{ice} versus SAD is in reasonable agreement with the measurements.

[44] On the basis of the supersaturation quenching timescale calculations presented above, the existence of s_{ice} values as high as 1.5 where ice surface areas are as high as 200 μm^2 cm^{-3} is unexpected. Close examination of the simulations reveals that the coincidence of high supersaturation and high ice surface area in these cases is caused by either (1) recent nucleation of ice crystals such that the surface area has accumulated but the crystals have not had time to deplete the supersaturation or (2) recent sedimentation of ice crystals into highly supersaturated air.

[45] The model results shown in Figure 19 suggest that within the cloud, regions near saturation or even below ice saturation should exist; whereas, the measurements shown in Figure 6 indicate little or no subsaturated air within the cloud. An important consideration here is that aircraft measurements can only sample a small fraction of the cloud volume. Figure 2 shows that for this case the WB-57 spent the vast majority of its time sampling the top part of the cloud layer. This sampling bias has important implications: since ice nucleation generally occurs near cloud top, and the crystals grow and fall with time, the upper part of the cloud will tend to have higher saturation ratios than the lower part of the cloud where surface areas are higher. If we limit our sampling of the model results to $\theta > 358$ K (approximately the top half of the simulated cloud), then nearly all of the subsaturated in-cloud regions are excluded. The subsaturated cloud regions apparent in Figure 19 were caused by ice crystals falling into subsaturated air at the bottom of the cloud. However, the s_{ice} values in the top half of the simulated cloud still approach 1.0 at high SAD in disagreement with the observations.

4.4.3. Impact of Increased Steady State Saturation Ratio

[46] As discussed above, we have also run a set of simulations with the enhanced steady state s_{ice} effect suggested by *Gao et al.* [2004]. The dependence of s_{ice} on SAD in this set of simulations is shown in Figure 20 (again with 5% standard deviation random values added to s_{ice}). As expected, s_{ice} converges toward about 1.3 at high SAD rather than approaching 1.0 as it did in the baseline simulations. This effect does, at least qualitatively, result in better agreement with the measured ice saturation ratios in the 13 July tropopause cloud layer. However, we do not feel that this particular case is conclusive evidence for an enhanced steady state vapor pressure over ice since the measured SAD values are not very high. The model results suggest that s_{ice} convergence toward a steady state value does not necessarily occur until surface areas exceed about 400 μm^2 cm^{-3}. The measured SAD in this cloud only reached about 1000 μm^2 cm^{-3}, and the SAD measurements are highly uncertain. In particular, maximum SAD values

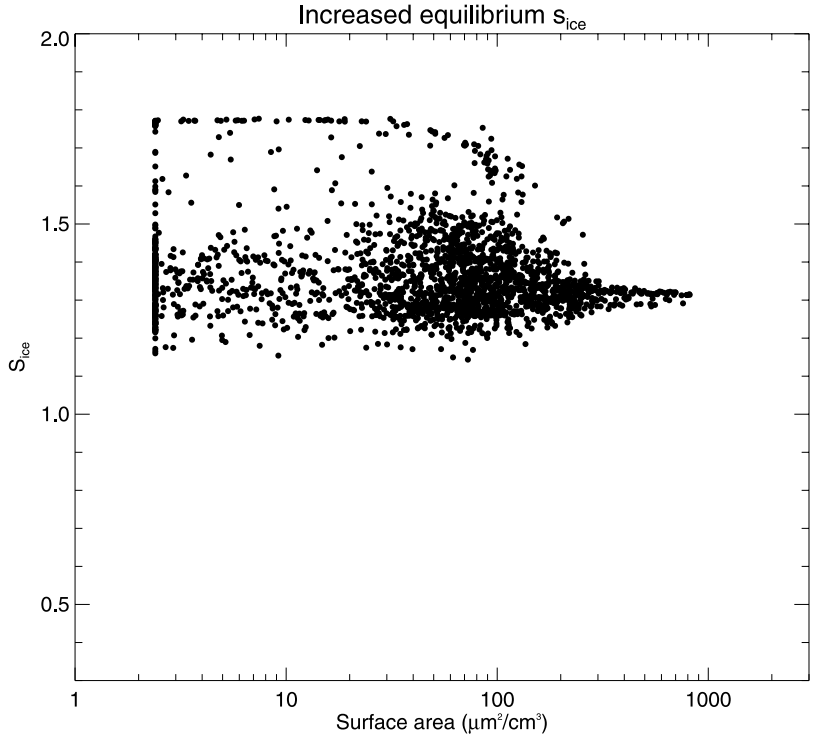

Figure 20. Ice saturation ratio plotted versus ice surface area for simulations with inhibited H_2O deposition on ice and correspondingly enhanced steady state H_2O vapor pressure over ice.

generated from different WB-57 instruments on this flight ranged from about 500–2000 μm^2 cm^{-3}.

5. Summary and Discussion

[47] We have presented measurements and model results of a thin cirrus layer at the subtropical tropopause. This study leads to the following conclusions: (1) Deep convection did not provide the ice crystals observed in the thin tropopause cloud layer. (2) The cloud layer formed because of cooling of air near the tropopause and in situ ice nucleation. (3) Cloud simulations forced by curtains of temperature versus height and time along trajectories can reproduce the observed cloud structure, ice crystal size distributions, and ice supersaturations. (4) Rapid temperature oscillations driven by gravity waves are required to explain the observed crystal size distributions and continuous cloud layer. (5) Using a deposition coefficient much smaller than unity (0.05) results in excessively numerous, small ice crystals and poor agreement with the observations. (6) In spite of rapid depletion of ice supersaturation within the cloud, regions of high ice surface area and high supersaturation occur because of recent nucleation of ice crystals and recent sedimentation of crystals into supersaturated layers. (7) Assuming steady state enhanced relative humidity in ice clouds at $T < 200$ K allows the model to reproduce the observed average supersaturation in the cloud layer; however, comparison between our simulations and the 13 July tropopause layer measurements do not provide conclusive evidence for steady state supersaturation in cold cirrus.

[48] The modeling approach used here neglects wind shear effects and just simulates the evolution of the cloud in an isolated vertical column assumed to remain coherent. This approach seems to work reasonably well for this case, primarily because the ice crystals sampled apparently formed no more than a few hours before the observations. The simulations here strongly indicate that the cloud formed in situ within the tropopause layer and are not left over from convectively generated cirrus upwind. This conclusion is supported by the water vapor isotope measurements as described by *Webster and Heymsfield* [2003].

[49] An important finding here is that the considerable scatter of saturation ratios in the cloud (s_{ice} values ranging from about 1 to 1.8) is consistent with the cloud simulations. The in-cloud relative humidity does not converge toward a steady state value until the surface area density exceeds about 400 μm^2 cm^{-3}. In this particular cloud, the surface areas only marginally exceed this threshold. Hence this cloud does not provide strong evidence for or against the existence of anomalously high steady state relative humidities in cold cirrus. However, the measurements in this tropopause cirrus layer are certainly not inconsistent with a steady state s_{ice} value of about 1.2–1.3.

[50] **Acknowledgments.** We thank Brian Ridley, David Knapp, Denise Montzka, and Frank Grahek for providing the nitric oxide measurements. We also thank Erik Richard for providing the ozone measurements and Andrew Dessler for providing the MODIS image. We are also grateful for useful discussions with Ru-shan Gao. This research was supported by both NASA's Atmospheric Chemistry Modeling and Analysis Program and NASA's Stratospheric Aerosol and Gas Experiment.

References

Baumgardner, D., H. Jonsson, W. Dawson, D. O'Connor, and R. Newton (2002), The Cloud, Aerosol and Precipitation Spectrometer (CAPS): A new instrument for cloud investigations, *Atmos. Res.*, *59–60*, 251–264.

Bertram, A. K., D. D. Patterson, and J. J. Sloan (1996), Mechanisms and temperatures for the freezing of sulfuric acid aerosols measured by FTIR extinction spectroscopy, *J. Phys. Chem.*, *100*, 2376–2383.

Comstock, J. M., T. P. Ackerman, and G. G. Mace (2002), Ground-based lidar and radar remote sensing of tropical cirrus clouds at Nauru Island: Cloud statistics and radiative impacts, *J. Geophys. Res.*, *107*(D23), 4714, doi:10.1029/2002JD002203.

Dessler, A. E., and P. Yang (2003), The distribution of tropical thin cirrus clouds inferred from Terra MODIS data, *J. Clim.*, *16*, 1241–1248.

Gao, R.-S., et al. (2004), Evidence that nitric acid increases relative humidity in low-temperature cirrus clouds, *Science*, *303*, 516–520.

Gettelman, A., W. J. Randel, F. Wu, and S. T. Massie (2002), Transport of water vapor in the tropical tropopause layer, *Geophys. Res. Lett.*, *29*(1), 1009, doi:10.1029/2001GL013818.

Gierens, K. M., M. Monier, and J.-F. Gayet (2003), The deposition coefficient and its role for cirrus clouds, *J. Geophys. Res.*, *108*(D2), 4069, doi:10.1029/2001JD001558.

Heymsfield, A. J. (1986), Ice particles observed in a cirroform cloud at −85°C and implications for polar stratospheric clouds, *J. Atmos. Sci.*, *43*, 851–855.

Jensen, E., and L. Pfister (2004), Transport and freeze-drying in the tropical tropopause layer, *J. Geophys. Res.*, *109*, D02207, doi:10.1029/2003JD004022.

Jensen, E. J., and O. B. Toon (1994), Ice nucleation in the upper troposphere: Sensitivity to aerosol number density, temperature, and cooling rate, *Geophys. Res. Lett.*, *21*, 2019–2022.

Jensen, E. J., O. B. Toon, H. B. Selkirk, J. D. Spinhirne, and M. R. Schoeberl (1996), On the formation and persistence of subvisible cirrus clouds near the tropical tropopause, *J. Geophys. Res.*, *101*, 21,361–21,375.

Jensen, E. J., L. Pfister, A. S. Ackerman, and A. Tabazadeh (2001), A conceptual model of the dehydration of air due to freeze-drying by optically thin, laminar cirrus rising slowly across the tropical tropopause, *J. Geophys. Res.*, *106*, 17,273–17,252.

Jensen, E. J., D. Starr, and O. B. Toon (2004), CRYSTAL-FACE mission, *Eos Trans. AGU*, *85*, 45–50.

Kärcher, B., and J. Ström (2003), The roles of dynamical variability and aerosols in cirrus cloud formation, *Atmos. Chem. Phys.*, *3*, 823–838.

Koop, T., H. P. Ng, L. T. Molina, and M. J. Molina (1998), A new optical technique to study aerosol phase transitions: The nucleation of ice from H_2SO_4 aerosols, *J. Phys. Chem. A*, *102*, 8924–8931.

Koop, T., B. Luo, A. Tsias, and T. Peter (2000), Water activity as the determinant for homogeneous ice nucleation in aqueous solutions, *Nature*, *406*, 611–614.

McGill, M. J., L. Li, W. D. Hart, G. M. Heymsfield, D. L. Hlavka, P. E. Racette, L. Tian, M. A. Vaughan, and D. M. Winker (2004), Combined lidar-radar remote sensing: Initial results from CRYSTAL-FACE, *J. Geophys. Res.*, *109*, D07203, doi:10.1029/2003JD004030.

Peter, T., et al. (2003), Ultrathin tropical tropopause clouds (UTTCs): I. Cloud morphology and occurrence, *Atmos. Chem. Phys.*, *3*, 1557–1578.

Pfister, L., et al. (2001), Aircraft observations of thin cirrus clouds near the tropical tropopause, *J. Geophys. Res.*, *106*, 9765–9786.

Richard, E. C., K. C. Aikin, E. A. Ray, K. H. Rosenlof, T. L. Thompson, A. Weinheimer, D. Montzka, D. Knapp, B. Ridley, and A. Gettelman (2003), Large-scale equatorward transport of ozone in the subtropical lower stratosphere, *J. Geophys. Res.*, *108*(D23), 4714, doi:10.1029/2003JD003884.

Ridley, B., et al. (2004), Florida thunderstorms: A faucet of reactive nitrogen to the upper troposphere, *J. Geophys. Res.*, *109*, D17305, doi:10.1029/2004JD004769.

Wang, P.-H., P. Minnis, M. P. McCormick, G. S. Kent, and K. M. Skeens (1996), A 6-year climatology of cloud occurrence frequency from Stratospheric Aerosol and Gas Experiment II observations (1985–1990), *J. Geophys. Res.*, *101*, 29,407–29,429.

Webster, C. R., and A. J. Heymsfield (2003), Water isotope ratios D/H, $^{18}O/^{16}O$, $^{17}O/^{16}O$ in and out of clouds map dehydration pathways, *Science*, *302*, 1742–1745.

Weinstock, E. M., E. J. Hintsa, A. E. Dessler, J. F. Oliver, N. L. Hazen, J. N. Demusz, N. T. Allen, L. B. Lapson, and J. G. Anderson (1994), New fast response photofragment fluorescence hygrometer for use on the NASA ER-2 and the Perseus remotely piloted aircraft, *Rev. Sci. Instrum.*, *22*, 3544–3554.

D. Baumgardner, Centro de Ciencias de la Atmosfera, Universidad Nacional Autonoma de Mexico, Circuito Exterior, Ciudad Universitaria, 04510 Mexico D.F., Mexico. (darrel@servidor.unam.mx)

T. Bui, E. Jensen, and L. Pfister, NASA Ames Research Center, MS 245-4, Moffett Field, CA 94035, USA. (ejensen@sky.arc.nasa.gov)

P. Lawson, Spec, Inc., 5401 Western Avenue, Boulder, CO 80301, USA. (plawson@specinc.com)

M. J. McGill, NASA Goddard Space Flight Center, Code 912, Greenbelt Road, Greenbelt, MD 20771-0001, USA. (matthew.j.mcgill@nasa.gov)

J. Pittman, J. Smith, and E. Weinstock, Department of Chemistry and Chemical Biology, Harvard University, 12 Oxford Street, Cambridge, MA 02138, USA. (elliot@huarp.harvard.edu)

A. Weinheimer, Atmospheric Chemistry Division, National Center for Atmospheric Research, P. O. Box 3000, Boulder, CO 80307-3000, USA. (wein@ncar.ucar.edu)